

Results of corrosive depositions on super-heater pipes

Author: Joseba Moreno, Eva Miller, Max Schmid

Release Status: FINAL

Date: 08 February 2022

Filename and version: NEWEST_D3.2.3_USTUTT



ACT2 NEWEST-CCUS project No 299683

This project NEWEST-CCUS is funded through the ACT programme (Accelerating CCS Technologies, Horizon2020 Project No 294766). Financial contributions made from The Research Council of Norway, (RCN), Norway; Bundesministerium für Wirtschaft und Energie (BMWi), Germany; Netherlands Ministry of Economic Affairs and Climate Policy, the Netherlands; and Department for Business, Energy & Industrial Strategy (BEIS) together with the Natural Environment Research Council (NERC) and the Engineering and Physical Sciences Research Council (EPSRC), United Kingdom are gratefully acknowledged.

This work has been jointly supported by the German Federal Ministry of Economic Affairs and Climate Action (BMWK) under Grant No. 03EE5020.

Document History

Location

This document is stored in the following location:

Filename	NEWEST_D3.2.3_USTUTT
Location	SCCS shared drive


Revision History

This document has been through the following revisions:

Version No.	Revision Date	Filename/Location stored:	Brief Summary of Changes
Version 1	08/02/2022	NEWEST_D3.2.3_USTUTT	

Authorisation

This document requires the following approvals:

AUTHORISATION	Name	Signature	Date
WP Leader or co-leader	Mario Ditaranto, Max Schmid		
Project Coordinator	Mathieu Lucquiaud		29/11/2022

Distribution

This document has been distributed to:

Name	Title	Version Issued	Date of Issue
			00/00/0000

© NEWEST-CCUS project, 2020

No third-party textual or artistic material is included in the publication without the copyright holder's prior consent to further dissemination by other third parties.

Reproduction is authorised provided the source is acknowledged.

Disclaimer

The information and views set out in this deliverable are those of the author(s) and do not necessarily reflect the official opinion of the Funders (RCN, BMWi, RVO, BEIS with NERC and EPSRC). Neither the Funders and bodies nor any person acting on their behalf may be held responsible for the use which may be made of the information contained therein.

Executive Summary

Within the NEWEST-CCUS project (Project-Nr.: 299683), different carbon capture, usage, and storage (CCUS) technologies are to be investigated in the context of Waste-to-Energy (WtE) plants, aiming at achieving net-negative CO₂ emissions.

A promising possibility in this regard comprise oxy-firing technologies applied to fluidized bed systems, which introduce the potential for higher efficiency with solid recovered fuel (SRF) combustion. During oxy-fuel combustion, the fuel is fired using pure oxygen instead of air as the primary oxidant. Since the nitrogen component of air is not heated, fuel consumption is reduced, and higher flame temperatures are possible. The justification for using oxy-fuel is thus to produce a CO₂-rich flue gas ready for sequestration.

This deliverable presents results from corrosion measurements performed at USTUTT's 200 kW CFBC facility in air and oxy-fuel combustion conditions. The samples collected in the facility in both settings evidence a clear attack by corrosion phenomena. During oxy-fuel operation, the short exposure time in combination with the relatively high chlorine content of the fuel led to an insufficient buildup of an oxidic protective layer (i.e., oxide scale). Consequently, chlorine diffused through the porous oxide scale and attacked the material surface directly. Besides, increased HCl values were measured during oxy-fuel operation, postulating HCl as the driver of the corrosion mechanism. In contrast, the HCl content in the flue gas during air-firing was relatively low. Hence, the strong corrosion attacks here were more likely to be originated from alkali salt deposits. On the other hand, chlorine and sulfur (partially) infiltrated the protective metal oxide layer in both combustion settings, breaking it off by side reactions between sulfates, chlorides, iron, and alkalis.

The results have shown that the atmospheres attained in both settings will not necessarily lead to fouling and heat transfer problems. However, a highly corrosive atmosphere has been determined in both combustion modes at the measured location.

Table of Contents

Executive Summary	4
List of abbreviations	6
List of symbols	6
1 Corrosion potential in WtE plants	7
2 Corrosion measurements at USTUTT’s 200 kW CFBC facility	7
2.1 Experimental methodology	7
2.1.1 Temperature-controlled deposition and material probe (short: corrosion probe)	8
2.1.2 Sample preparation	9
2.1.3 Sample analysis by SEM-BSE/EDX	9
2.2 Results and discussion	10
2.2.1 Air combustion	11
2.2.2 OXY28 (Oxy-fuel combustion with 28 vol% inlet O ₂)	15
2.3 Conclusions	19
Acknowledgements	20
References	20
Annex	22
Slag formation during the OXY28 combustion case	22
Sample analysis by SEM-BSE/EDX	24
Results and discussion	24
Conclusions	30
Analysis of solid samples during corrosion measurements	30
Air combustion	30
OXY28 (Oxy-fuel combustion with 28 vol% inlet O ₂)	31

List of abbreviations

Acronym	Description
an	“Analysenfeucht” (at analysis conditions)
ar	As received
BSE	Backscattered electron
CFB	Circulating fluidized bed
CFBC	Circulating fluidized bed combustor
EDX	Energy-dispersive X-ray spectroscopy
SE	Secondary electron
SEM	Scanning electron microscopy
SRF	Solid recovered fuel
wf	Water free
WtE	Waste to energy

List of symbols

Symbol	Description
T	Temperature (°C)
t	Time, duration (hh:mm)
x_i	Mass fraction of component “i” (kg/kg)

1 Corrosion potential in WtE plants

Because of its non-homogeneous and varying nature, waste is commonly regarded as a challenging fuel for power generation and CO₂ capture technologies [2]. Waste-derived fuels usually present a higher content in ash combined with an enrichment of undesirable components such as heavy metals and chlorine. Consequently, Waste-to-Energy (WtE) facilities typically suffer from challenges associated with low-grade fuels such as slagging, bed agglomeration, and corrosion [1,9,10].

In the last decades, high-temperature corrosion has gained increasing attention due to the comparatively high chlorine content of alternative fuels [4]. A high chlorine fuel content combined with alkali metals (i.e., Na, K) and heavy metals (i.e., Pb, Zn) might promote chloride-induced corrosion under certain operation conditions [6,8]. Hence, the latter aspect has remained a significant challenge in WtE plants that are operated with waste-derived fuels.

The experiments presented in the following deliverable aim at addressing the corrosion potential of circulating fluidized bed combustors (CFBC) powered by mono-combustion of solid recovered fuels (SRF) [3]. The work evaluates the influence of combustion atmosphere upon corrosion using a metal sample carrier commonly employed in circulating fluidized bed (CFB) facilities (i.e., X20CrMoV11-1). The methodology is based on a temperature-controlled deposition and material probe, a well-known technique for determining corrosion potential in waste incinerators [5,7]. A detailed description of both the pilot facility and the solid materials is included in Deliverable 3.2.2. In the following, the methodology and results obtained during corrosion measurement are presented.

2 Corrosion measurements at USTUTT's 200 kW CFBC facility

2.1 Experimental methodology

Industrial waste incineration plants are operated with low steam temperatures to prevent the formation of highly corrosive deposits such as alkaline salts. As the fluidized bed cooler of a CFBC is not exposed to waste combustion flue gas atmosphere, it is expected that none or much fewer such deposits will be formed, allowing for higher steam temperatures and higher efficiencies without higher corrosion. This matter has been investigated via equilibrium ash simulations with the thermochemical software FactSage® and experimentally by analysis of probe deposits at the 200 kW CFBC pilot facility.

Due to technical limitations, the corrosion probe could not be installed at the initially planned location (i.e., loop seal, simulated fluidized bed cooler). Instead, the probe was placed at the primary cyclone, aiming at measuring corrosion under very low particle concentration conditions (see Figure 1). Besides, sampling of solids was conducted in the bag filter, after the protective cyclone, and in the loop seal.

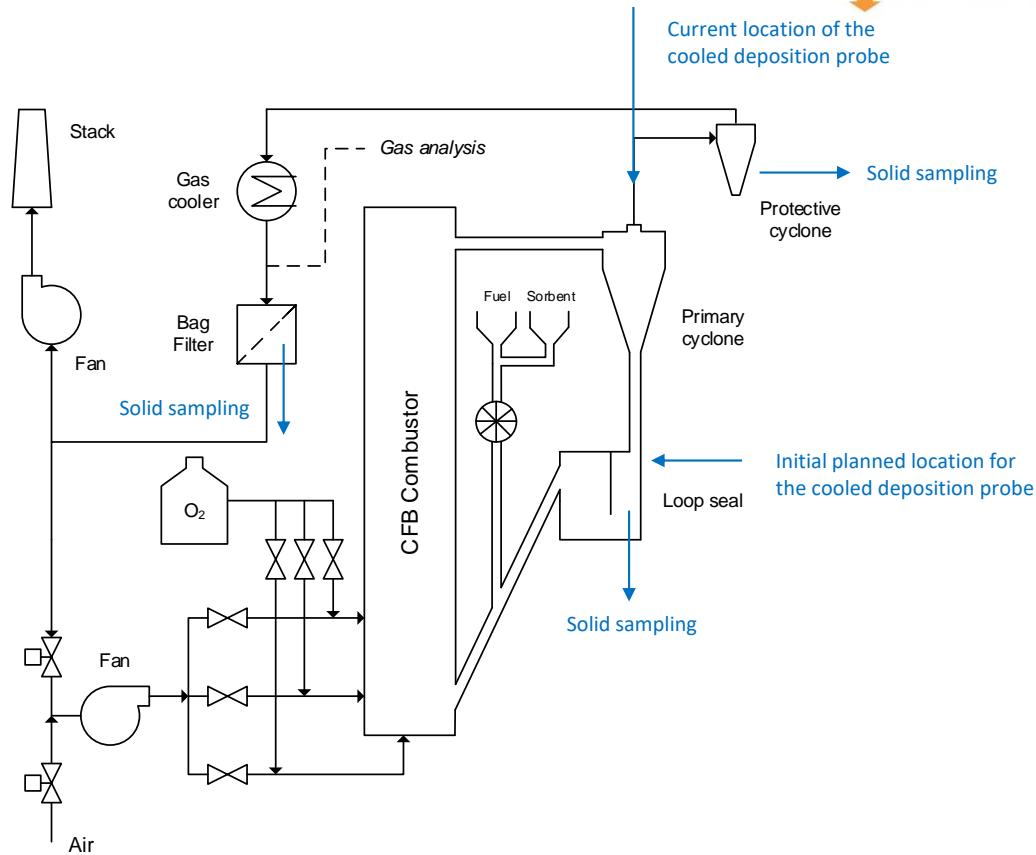


Figure 1. Schematic of the 200 kW CFBC pilot facility at USTUTT (blue: probe locations and sampling points)

2.1.1 Temperature-controlled deposition and material probe (short: corrosion probe)

For the characterization of deposits and their interactions with the base materials on flue gas touched heating surfaces (evaporator/superheater), an air-cooled probe can be inserted at various plant locations. In these tests, the primary cyclone has been chosen to apply the corrosion probe.

The air-cooled probe is applied to collect deposit ash as well as check corrosion (mechanisms) of test materials. Pressurized air is used as a direct coolant to control the tube surface temperature, which is measured by thermocouples. The controlling of the cooling efficiency results from regulating valves. The cooled probe simulates the boiler heat exchanger surfaces. The deposition that forms on the temperature-controlled material surface is called the initial layer. The condensable ash species in the surrounding hot flue gas, fine fly ash particles, and aerosols are transported to the cooled surface due to thermophoresis as well as molten / semi-molten and solid fly ash particles are collected due to inertial impaction. The latter described mechanisms represent the deposit formation over the cooled probe. The deposit samples collected during the experiments were prepared for electron microscopic image analysis. Figure 2 shows some pictures of the probe to get an impression of how the measurement is done.



Figure 2. Exemplary images of cooled deposit collections

2.1.2 Sample preparation

After exposure, the samples (i.e., material rings) are embedded directly with epoxy resin to freeze further reactions of the elements in the depositions and material surfaces and fix the depositions. To analyze the samples by means of scanning electron microscopy and energy-dispersive X-ray spectroscopy (SEM/EDX) on corrosion mechanisms and slugging, cross-sections of the material samples were embedded again with epoxy resin. Furthermore, water-free grinding and polishing work finished the preparation. Figure 3 illustrates an example of a cooled deposition sample on a steel pipe prepared for SEM/EDX analysis.

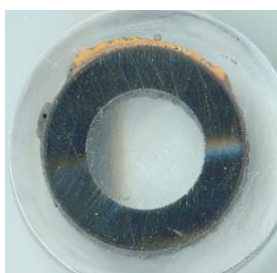


Figure 3. Example of sample ring prepared for SEM/EDX analysis

2.1.3 Sample analysis by SEM-BSE/EDX

In the next section, the results of the microscopic investigation of the cooled deposit samples are presented. The standard element map of the analyzed deposit consists of a backscattered electron (BSE) image of the deposit. It is a cross-section view of the section of the metal sample carrier. The

BSE image of the deposit sample cross-section was generated to visually evaluate the morphology of deposits. The intensity of the signal depends primarily on the average atomic number of the material. Heavy elements provide strong backscattering so that corresponding areas appear bright. Areas with lighter elements, on the other hand, appear darker.

SEM/EDX analysis was performed to generate element maps to evaluate the qualitative distribution of major elements present in the deposits. This distribution supplements the standard element map produced for each test. In the corner of the image, the chemical symbol for the element discovered in the deposit is placed. The concentration scale supports a standard element map to assess the semi-quantitative distribution of major elements, as well as point out their locations. Various points/areas in the cross-section of the sample are analyzed by SEM-EDX scan to evaluate the distribution of elements.

2.2 Results and discussion

The corrosion sample was taken using the previously described temperature-controlled probe (see chapter 2.1.1). The probe is equipped with a replaceable metal sample attached with a thermocouple. The temperature of the metal is controlled by airflow. The temperature at the surface of the replaceable metal probe was kept at approx. 480 °C. The chosen metal sample was an X20CrMoV11-1 ring for each case. Table 1 shows the composition of the materials.

Table 1. Elemental composition of used metal sample (1,4922; X20CrMoV11-1)

X_C (wt%)	X_{Si} (wt%)	X_{Mn} (wt%)	X_P (wt%)	X_S (wt%)	X_{Cr} (wt%)	X_{Mo} (wt%)	X_{Ni} (wt%)	X_V (wt%)	X_{Fe} (wt%)
0,17- 0,23	0,5	1,0	0,025	0,015	10,0- 12,2	0,8- 1,2	0,3- 0,8	0,25- 0,35	rest

To evaluate the buildup of the initial deposit layer and potential corrosion risk, the metal sample was exposed to different combustion conditions. Table 2 shows an overview of the test cases, the material and flue gas temperature, fuel, location and exposure time.

Table 2. Superheater material samples, material and flue gas temperature, fuel, location and exposure time

Case	Fuel	Material	Location	$T_{material}$ (°C)	$T_{fluegas}$ (°C)	$t_{duration}$ (hh:mm)
Air	SBS®1	X20CrMoV11-1 Sample: 60 mm length x 38 mm diameter	Primary cyclone	480	Ca. 750	10:30
OXY28	SBS®1	X20CrMoV11-1 Sample: 60 mm length	Primary cyclone	480	Ca. 690	00:50

		x 38 mm diameter				
--	--	------------------	--	--	--	--

Figure 4 shows the samples after removal from the cyclone. The specimens show strong corrosion characteristics. The deposit has completely split off during the air combustion case. In addition, the sample collected during the OXY28 case shows clear corrosion even after 50 min of exposure. The split-off depositions were reconstructed on the material for photography, embedding, and analysis.



X20CrMoV11-1	
Air	
OXY28	

Figure 4. Overview of samples after removal of combustion chamber

2.2.1 Air combustion

Figure 5 shows the embedded and polished cross-section of the metal sample, which was exposed with the corrosion probe at a 480 °C surface temperature and a flue gas temperature of 750 °C for 10 hours 30 minutes. Some areas (i.e., blue boxes) were analyzed by SEM/EDX. The Figure shows the BSE pictures of these areas. In the following sections, a selection of these areas is analyzed and evaluated in more detail.

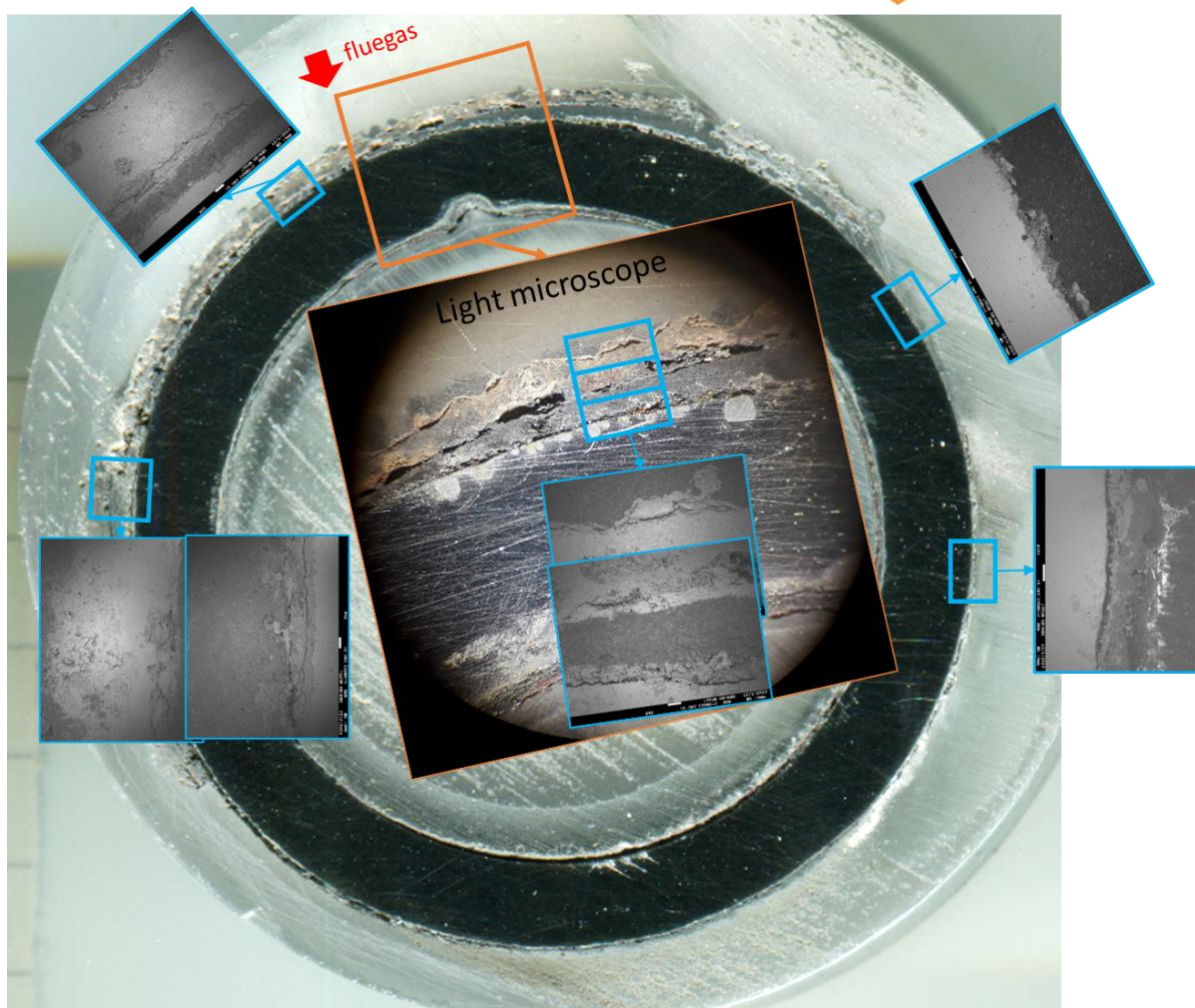


Figure 5. Cross-section of the metal sample and areas with BSE images during the air combustion test

Figure 6 shows an overview of the deposit structure from transition material to deposit and deposit to embedding material (resin) at the “luv” side (flue gas). Since the deposit split off after removal of the pilot plant, there is another layer of embedding material between the oxide layer on the material and the deposit. For analysis, the off-cut pieces of deposition were reconstructed on the specimen again. The overview shows the different layers: attacked material, porous oxide scales, and compact deposit.

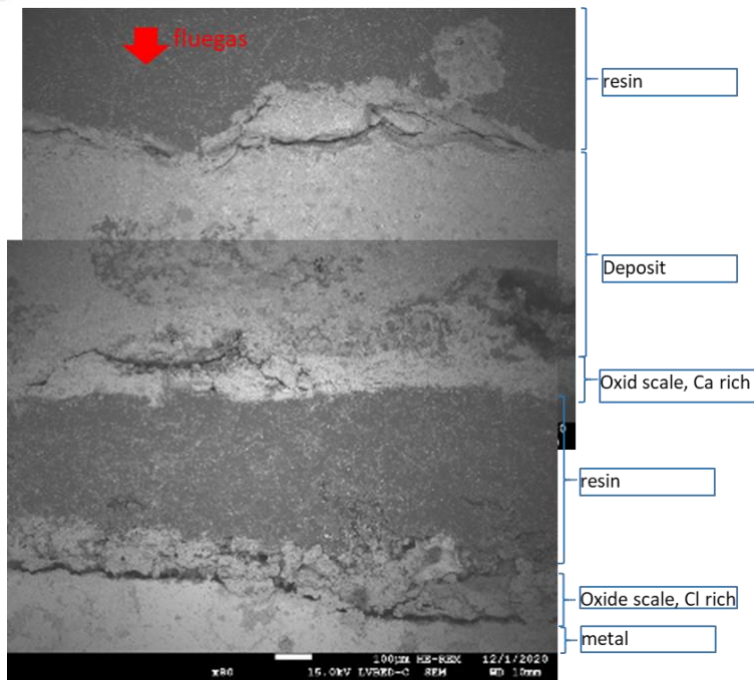


Figure 6. Overview of the deposit structure during the air combustion test

Figure 7 and Figure 8 show the element mappings of the areas shown in the middle of Figure 5 and Figure 6. The oxide scale is split into two layers. One adheres to the metal; the second part sticks to the deposit. Due to the high Cl content in the fuel of 0.49 wt%, the Cl was able to spread in the deposit and diffuse through the oxide layer to the pure metal surface. The alkalis Na, K and Ca, and also Al are homogeneously distributed in the deposit. Many small Si particles are embedded in the deposit. S is also found homogeneously distributed but in small amounts. Cl mainly compounds with K and Fe. Possible corrosive compounds: KCl, NaCl, CaCl₂, K₂SO₄, Na₂SO₄, CaSO₄.

These chlorine salts and the release of Cl₂ by sulfation can lead to the formation of FeCl_x below the porous oxide scale.

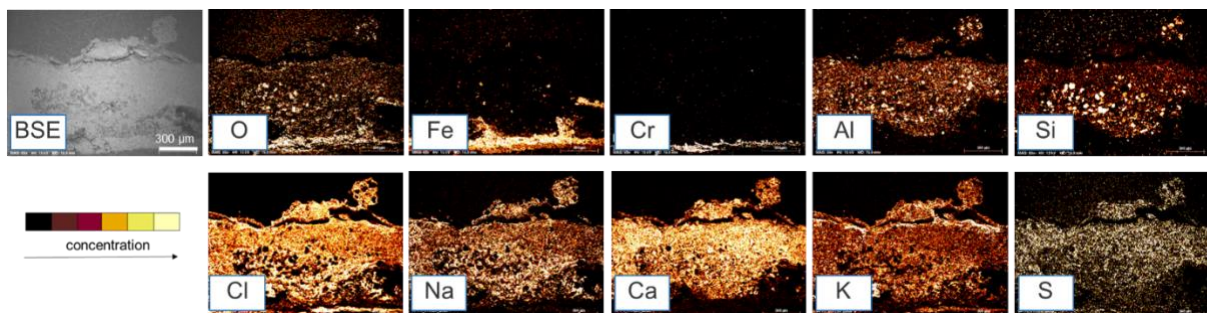


Figure 7. SEM/EDX element mappings; air combustion case; upper deposit part

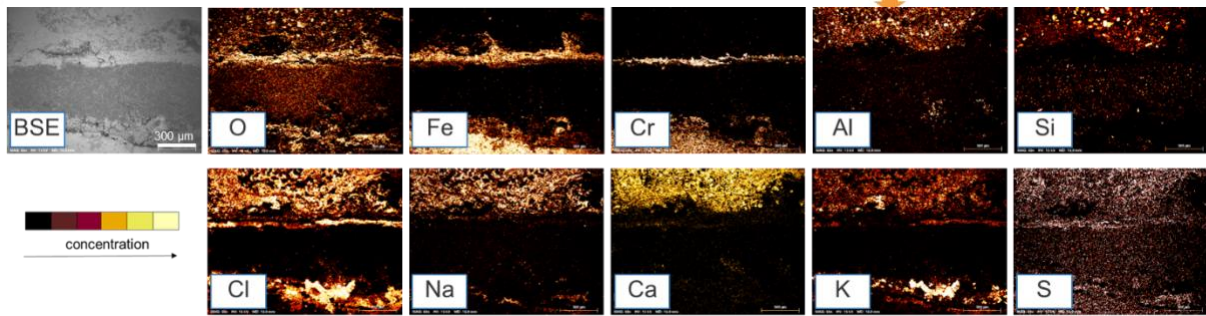


Figure 8. SEM/EDX element mappings; air combustion case; lower deposit part

Figure 9 shows the compositions of the corrosive elements: Fe and Cl, K and Cl, Na and Cl, and Ca and Cl. The images show only the positions where the two selected elements are bound together. The corrosion front directly on the material surface is noticeable (FeCl_x and KCl). Alkali salts are homogeneously distributed in the deposit.

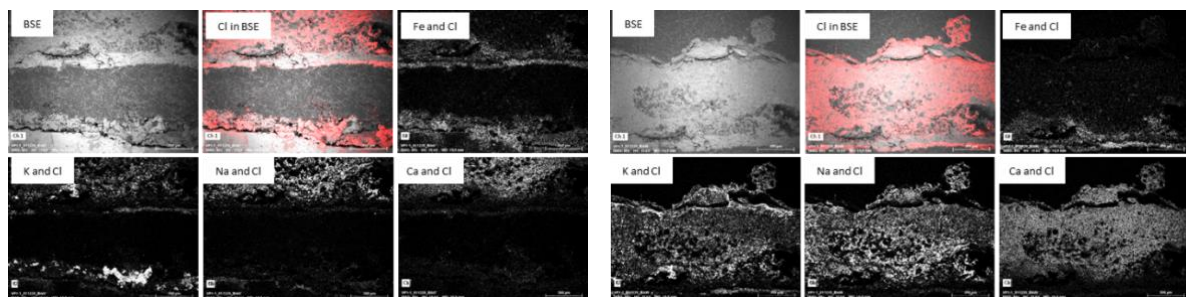


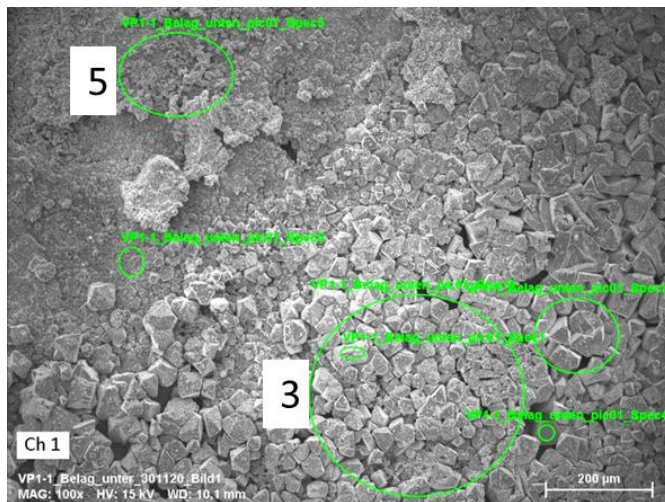
Figure 9. Compositions of the corrosive elements during the air combustion test: Fe+Cl, K+Cl, Na+Cl and Ca+Cl; left: lower deposit part; right: upper deposit part

In the following section, the lower part of a split-off piece of deposit, which used to adhere to the surface of the material (**Figure 10**), is examined by SEM/EDX. The deposit could no longer adhere to the base material due to the formation of FeCl_x particles and the associated dissolution and splitting of the oxide layer. Cl and partially also S infiltrate the protective metal oxide layer and break it off both by reactions taking place, such as sulfation, between sulfates, chlorides, iron, and alkalis and by the increase in volume during the formation of solid iron chlorides. Furthermore, thermal stresses also affect the adhesion of the oxide layers and coatings when the probe is removed from the plant.



Figure 10. Part of deposit during the air combustion case

In **Figure 11**, you can see the underside of the deposit piece. The crystalline particles consisting mainly of Fe and Cl analyzed by SEM/EDX are clearly visible.



Element	Spectrum 3	Spectrum 5
	Mass Norm. [%]	Mass Norm. [%]
O	15,61	17,07
Fe	67,56	54,09
Si	0,19	0,57
Na	2,07	3,35
Al	0,12	-
Cl	6,51	11,12
K	3,74	6,08
Ca	1,51	1,92
Cu	1,24	1,04
S	0,76	1,00
Cr	0,68	3,75
Sum	100	100
	Normalised to 100%	

Figure 11. SEM/BSE of underside of the deposit piece; SEM/EDX spectra, underside of the deposit sample, Spectrum 3 and 5. Air combustion case

2.2.2 OXY28 (Oxy-fuel combustion with 28 vol% inlet O₂)

Figure 12 and Figure 16 show the embedded and polished cross-section of the metal sample, which was exposed with the corrosion probe at a 480 °C surface temperature and a flue gas temperature of 850 °C for 50 minutes. Some areas (blue boxes) were analyzed by SEM/EDX. The Figures show the BSE pictures of these areas. In the following sections, a selection of these areas is analyzed and evaluated in more detail.

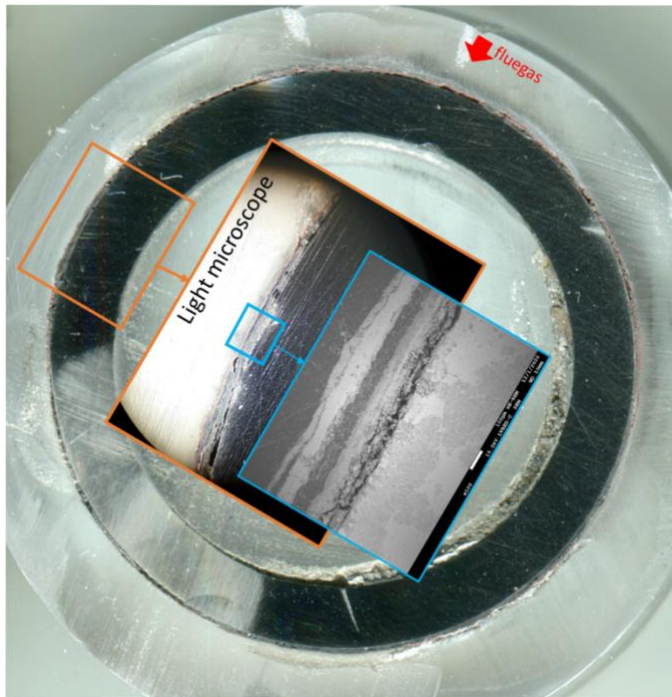


Figure 12. Cross-section of the metal sample and analyzed area with BSE image at the OXY28 case

Figure 13 shows an overview of the deposit structure from transition material to deposit and deposit to embedding material (resin) at the “luv” side (flue gas). Since the deposit split off after removal of the pilot plant, there is another layer of embedding material between the oxide layer on the material and the deposit. The metal indicates attacks.

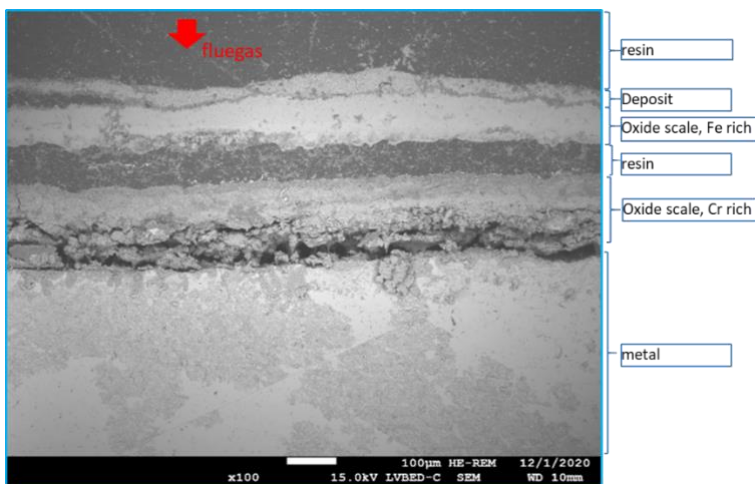


Figure 13. Overview of the deposit structure at the “luv” side during the OXY28 case

Figure 14 shows the element mappings of the areas shown in **Figure 12** and **Figure 13**. The oxide scale is split into two layers. One adheres to the metal; the second part sticks to the small deposit. Due to the high Cl content in the fuel of 0.49 wt%, the Cl was able to spread in the deposit and diffuse through the oxide layer to the pure metal surface. The alkalis Na, K, and Ca are homogeneously distributed in the deposit. Many small Si particles are embedded in the deposit. S is also found homogeneously distributed. Cl mainly compounds with K, Na Ca, and Fe. Possible corrosive compounds: KCl, NaCl, CaCl₂, K₂SO₄, Na₂SO₄, CaSO₄.

These chlorine salts and the release of Cl_2 by sulfation can lead to the formation of FeCl_x below the porous oxide scale. At the material surface, Cl is only found in combination with Fe. S is detected in the oxide scale. Here too, as in the sample from the air combustion case, spalling of the protective oxide layer occurs. Here it can be seen that the Fe oxide layer dissolves, while the Cr oxide layer appears more stable. However, this also begins to dissolve due to the penetration of Cl.

The structures on the surface of the metal were formed after the grinding process. Hygroscopic compounds led to droplet formation on the surface. Fe oxides were formed.

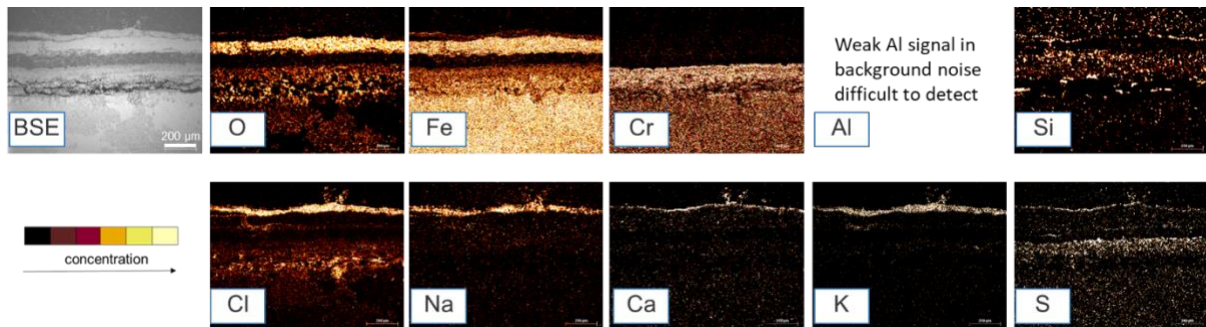


Figure 14. SEM/EDX element mappings at the “luv” side during the OXY28 case

Figure 15 shows the compositions of the corrosive elements: Fe and Cl, K and Cl, Na and Cl, and Ca and Cl. The images show only the positions where the two selected elements are bound together. The corrosion front directly on the material surface is noticeable (FeCl_x). Alkali salts are homogeneously distributed in the small deposit.

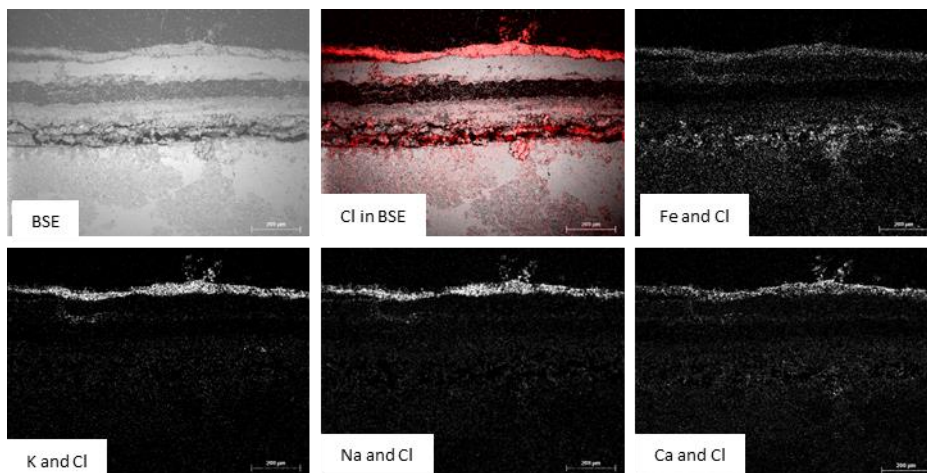


Figure 15. Compositions of the corrosive elements at the “luv” side: Fe+Cl, K+Cl, Na+Cl and Ca+Cl; OXY28 combustion case

Figure 16 shows another position analyzed in the sample collected during the OXY28 case (i.e., sideways). A reddish layer can be seen in the light microscope image, which indicates the presence of hematite.

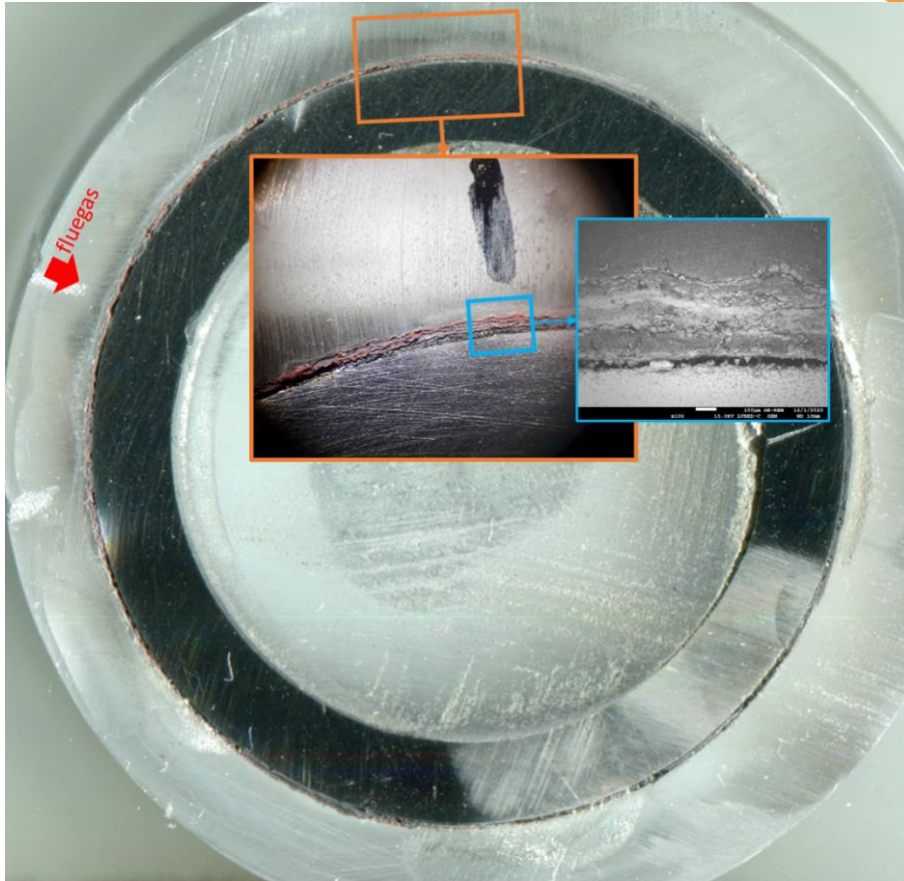


Figure 16. Cross section of the metal sample and analyzed area with BSE image; OXY28 combustion case

Figure 17 shows an overview of the deposit structure from transition material to deposit and deposit to embedding material (resin), sideways. Since the deposit split off after removal of the pilot plant, there is another layer of embedding material between the oxide layer on the material and the deposit. The deposit and oxides scale look very porous and broken.

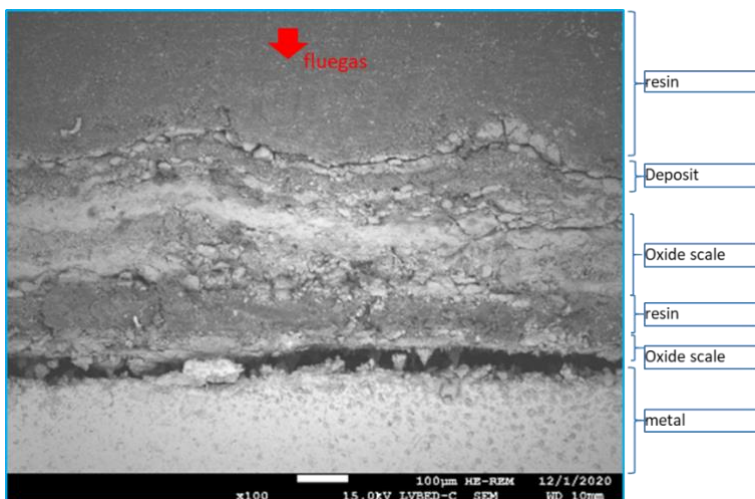


Figure 17. Overview of the deposit structure at the OXY28 case, sideways

Figure 18 shows the element mappings of the areas shown in **Figure 16** and **Figure 17**. The oxide scale is split into two layers. A thick, iron-rich area represents the hematite interspersed layer.

Another, Cr-rich zone, adheres to the metal. After a short time of only 50 minutes, FeCl_x particles are found in the gap between the material surface and the oxide scale. The alkalis Na and K are homogeneously distributed in the small deposit. Ca was found homogeneously distributed together with S in small amounts in deposit and oxide scale. Cl mainly compounds with K, Na, and Fe. Possible corrosive compounds: KCl, NaCl, CaSO_4 .

These chlorine salts and the release of Cl_2 by sulfation can lead to the formation of FeCl_x below the porous oxide scale. At the material surface, Cl is only found in combination with Fe. S is detected in the oxide scale.

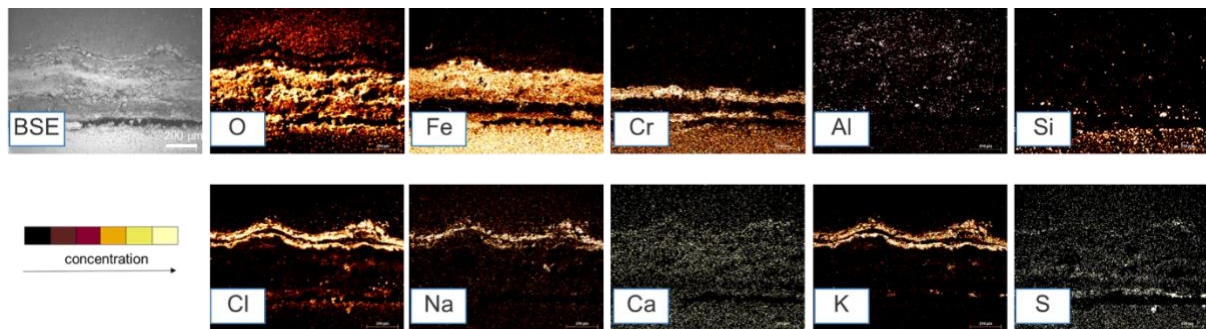


Figure 18. SEM/EDX element mappings during the OXY28 case, sideways

Figure 19 shows the compositions of the corrosive elements: Fe and Cl, K and Cl, Na and Cl, and Ca and Cl. The images show only the positions where the two selected elements are bound together. The corrosion front directly on the material surface is noticeable (FeCl_x). Alkali salts are homogeneously distributed in the small deposit.

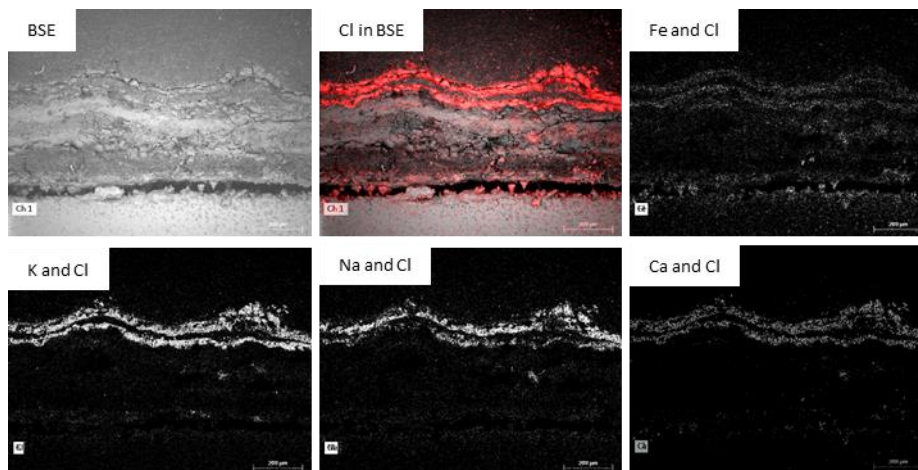


Figure 19. Compositions of the corrosive elements during the OXY28 case, sideways: Fe+Cl, K+Cl, Na+Cl and Ca+Cl

2.3 Conclusions

Due to technical limitations, the probe could not be installed at the initially planned location (i.e., loop seal, simulated fluidized bed cooler). Instead, the probe was placed at the primary cyclone, aiming at measuring corrosion under low particle concentration conditions. Besides, sampling of solids was conducted in the bag filter, after the protective cyclone, and in the loop seal.

Corrosion phenomena clearly attacked the cooled deposition samples in both settings. The short exposure times and the high Cl content in the fuel led to an insufficient buildup of an oxidic protective layer (oxide scale). Cl diffused through the porous oxide scale and attacked the material surface. The Cr content was not high enough to quickly build up a protective layer. Cl and partially also S infiltrated the protective metal oxide layer in both combustion modes and broke it off both by side reactions between sulfates, chlorides, iron, and alkalis and by the increase in volume during the formation of solid iron chlorides. Furthermore, thermal stresses also affected the adhesion of the oxide layers and coatings when the probe was removed from the plant.

The HCl content in the flue gas at air combustion was relatively low. Therefore, the strong corrosion attacks were more likely to originate from alkali salt deposits. Despite the cyclone, Cl reached the sample in alkali-rich ashes (particles/melt). A strongly increased HCl value was measured during the OXY28 case. In contrast to air combustion, HCl seemed to be the driver of the corrosion. The gaseous species reached the unprotected metal surface directly. The corrosion damage occurred in a very short time. The sulfur content in the fuel and the related formation of SO₂/SO₃ in both settings was too low to sulfate the Cl salts already in the flue gas and convert the compounds into more harmless sulfates.

Based on the solids sampled from the loop seal (see Annex) it is difficult to determine the corrosion potential occurring in such a unit. The samples taken in air-firing conditions reveal an increasing tendency of sulphur (i.e., SO₃) in the solids, whereas the chloride content of the solids shows a rather constant behavior. Furthermore, the loop seal is not equipped with a gas measurement device, so it is not possible to determine the volume concentration of HCl in the atmosphere. Last but not least, it should be noted that erosion is also occurring simultaneously, which difficult the assessment of corrosion potential with the loop seal. Further work should be undertaken to address the knowledge gaps addressed in this study.

The atmospheres of both settings did not lead to fouling problems and, therefore, to heat transfer problems. However, there was a highly corrosive atmosphere at the measurement location in each case.

Acknowledgements

The authors acknowledge the financial support by the German Federal Ministry of Economic Affairs and Climate Action (BMWK) under Grant No. 03EE5020. The authors would also like to thank the academic and technical staff of the IFK's department "Dezentralized Energy Conversion" for their support. Special thanks go to the team of IFK's "Laboratory for Fuels, Ashes and Slag" for supporting this work with lab analyses of fuels and sorbents.

References

- [1] Al-Qayim K, Nimmo W, Hughe KJ, Pourkashanian M. Effect of oxy-fuel combustion on ash deposition of pulverized wood pellets. *Biofuel Res. J.* 2019;6(1):927–36. <https://doi.org/10.18331/BRJ2019.6.1.4>.
- [2] Ditaranto M, Becidan M, Stuen J. Opportunities for CO₂ Capture in the Waste-to-Energy Sector. *Waste Management*. Thomé-Kozmiensky Verlag GmbH. 2019;9:319–328.
- [3] ISO 21640:2021. Solid recovered fuels - Specifications and classes. Geneva, Switzerland, 2021: International Organization for Standardization.
- [4] Kimmel J (ed.). *Dampfkessel in Hausmüll- bzw. Restmüll-Verbrennungsanlagen*; 1994.

- [5] Ludmilla Krumm MG. VOKos - Effizienzsteigerung durch verfahrenstechnisch optimierende Korrosionsschutzkonzepte in Verbrennungsanlagen mit heterogenen Festbrennstoffen: Förderkennzeichen: 03X3589C. DECHEMA Forschungsinstitut 2017(DECHEMA Forschungsinstitut).
- [6] Ott D. Hochtemperaturkorrosion in Müllverbrennungsanlagen - Die Kinetik der Chlorfreisetzung als bestimmender Faktor. Universität Augsburg 2017(Universität Augsburg).
- [7] S. Maisch, R. Warnecke, S. Horn, F. Haider. Weiterentwicklung und Optimierung einer online Korrosionssonde. Bayrisches Staatsministerium für Umwelt und Gesundheit 2010.
- [8] Sorell G. The role of chlorine in high temperature corrosion in waste-to-energy plants. *Materials at High Temperatures* 1997;14(3):207–20. <https://doi.org/10.1080/09603409.1997.11689546>.
- [9] Wu J, Wang Y, Han J, Li X, Yu D, Xu M et al. Ash Formation and Deposition in Oxy-fuel Combustion of Rice Husk, Coal, and Their Blend with 70% Inlet O₂. *Energy Fuels* 2020;34(1):890–9. <https://doi.org/10.1021/acs.energyfuels.9b03129>.
- [10] Yang X, Szuhánszki J, Tian Y, Ingham D, Ma L, Pourkashanian M. Understanding the effects of oxyfuel combustion and furnace scale on biomass ash deposition. *Fuel* 2019;247:36–46. <https://doi.org/10.1016/j.fuel.2019.03.031>.

Annex

Slag formation during the OXY28 combustion case

Slag samples were taken after the OXY28 combustion test from the bottom ash of the CFB combustor. One of the samples was prepared as cross-section for electron microscopic image analysis (Figure 20). The chemical composition of such slag sample is given in Table 3.

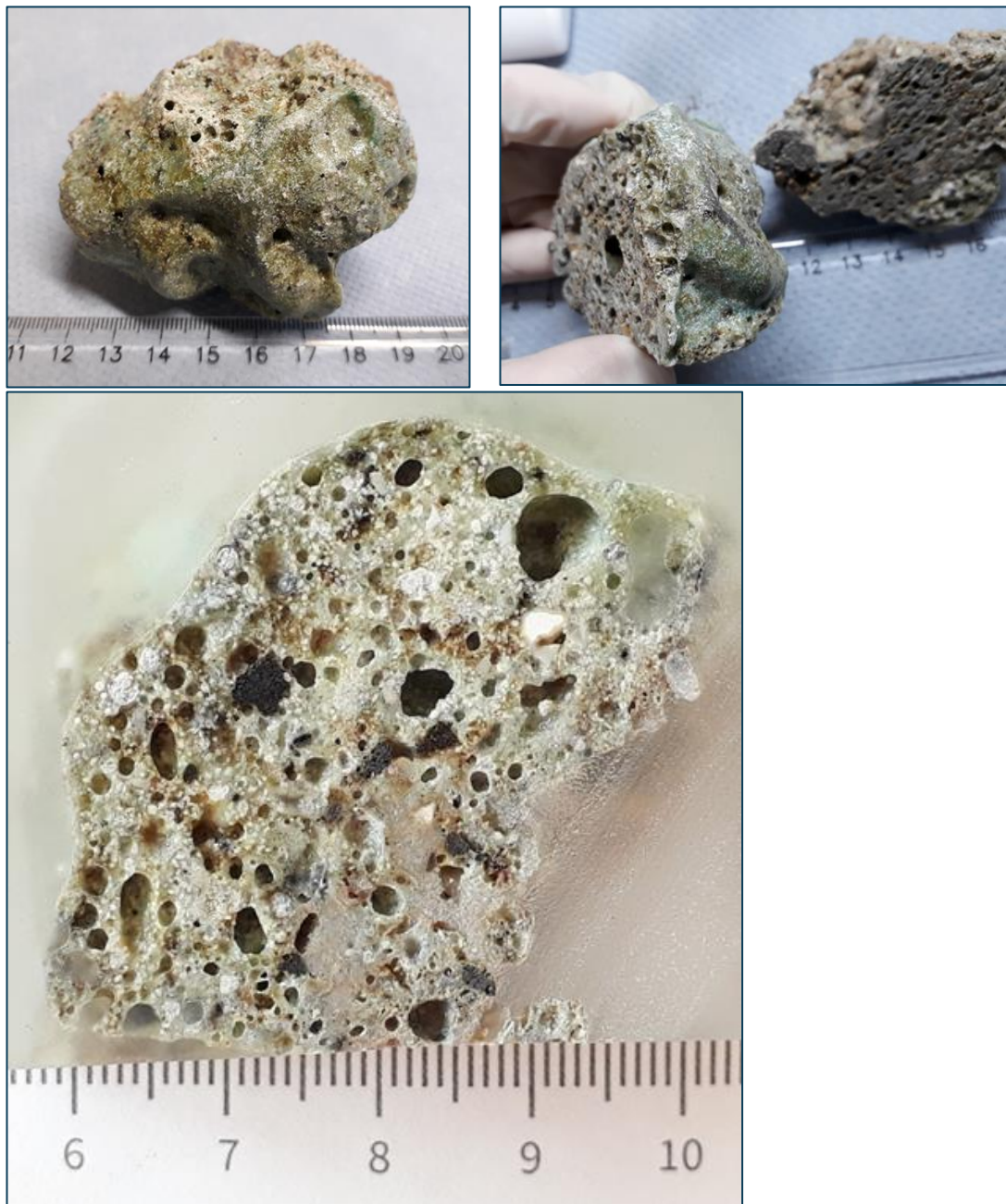


Figure 20. Piece of slag out of bottom ash after the OXY28 combustion test

Table 3. Composition of slag piece

Proximate analysis	Value/Range (ar)
Moisture (wt%)	< 0,05
Ash, O ₂ +550 °C (wt%)	100
Main elements	Value/Range (wf)
SiO ₂ (wt%)	68,2
CaO (wt%)	12,3
Al ₂ O ₃ (wt%)	5,93
Na ₂ O (wt%)	5,82
MgO (wt%)	2,51
Fe ₂ O ₃ (wt%)	2,36
K ₂ O (wt%)	2,07
TiO ₂ (wt%)	1,30
Trace elements	Value/Range (wf)
Mn (mg/kg)	646
Ni (mg/kg)	583
S (mg/kg)	419
Pb (mg/kg)	362
Sr (mg/kg)	247
Sb (mg/kg)	115
Mo (mg/kg)	60,7
V (mg/kg)	33,3
Co (mg/kg)	31,3
As (mg/kg)	26,9
Tl (mg/kg)	9,64

Cd (mg/kg)	1,88
Be (mg/kg)	0,93
Additional elements	Value/Range (wf)
P ₂ O ₅ (wt%)	0,494
Cu ₂ O (wt%)	0,373
Cr ₂ O ₃ (wt%)	0,301
ZnO (wt%)	0,207

Sample analysis by SEM-BSE/EDX

In the next section, the results of the microscopic investigation of the slag sample are presented. The standard element map of the analyzed deposit consists of a backscattered electron (BSE) image and a secondary electron (SE) image of the deposit. The BSE image of the slag sample cross-section was generated to visually evaluate the morphology of the sample. The intensity of the signal depends primarily on the average atomic number of the material. Heavy elements provide strong backscattering so that corresponding areas appear bright. Areas with lighter elements, on the other hand, appear darker.

SEM/EDX analysis was performed to generate element maps to evaluate the qualitative distribution of major elements present in the deposits. This distribution supplements the standard element map produced for each test. In the corner of the image, the chemical symbol for the element discovered in the deposit is placed. The concentration scale supports a standard element map in order to assess the semi-quantitative distribution of major elements, as well as point out their locations. Various points/areas in the cross-section of the sample are analyzed by SEM-EDX scan to evaluate the distribution of elements. This analysis spectra method is semi-quantitative. C is not calculated. The remaining detected elements are normalized to 100 %.

Results and discussion

Figure 21 shows the embedded and polished cross-section of the slag sample, which was sampled at the bottom ash container of the CFB combustor at the OXY28 test with a flue gas temperature of 850 °C. Some areas (blue boxes) were analyzed by SEM/EDX. The Figures show the BSE and SE pictures of these areas. In the following sections, a selection of these areas is analyzed and evaluated in more detail.

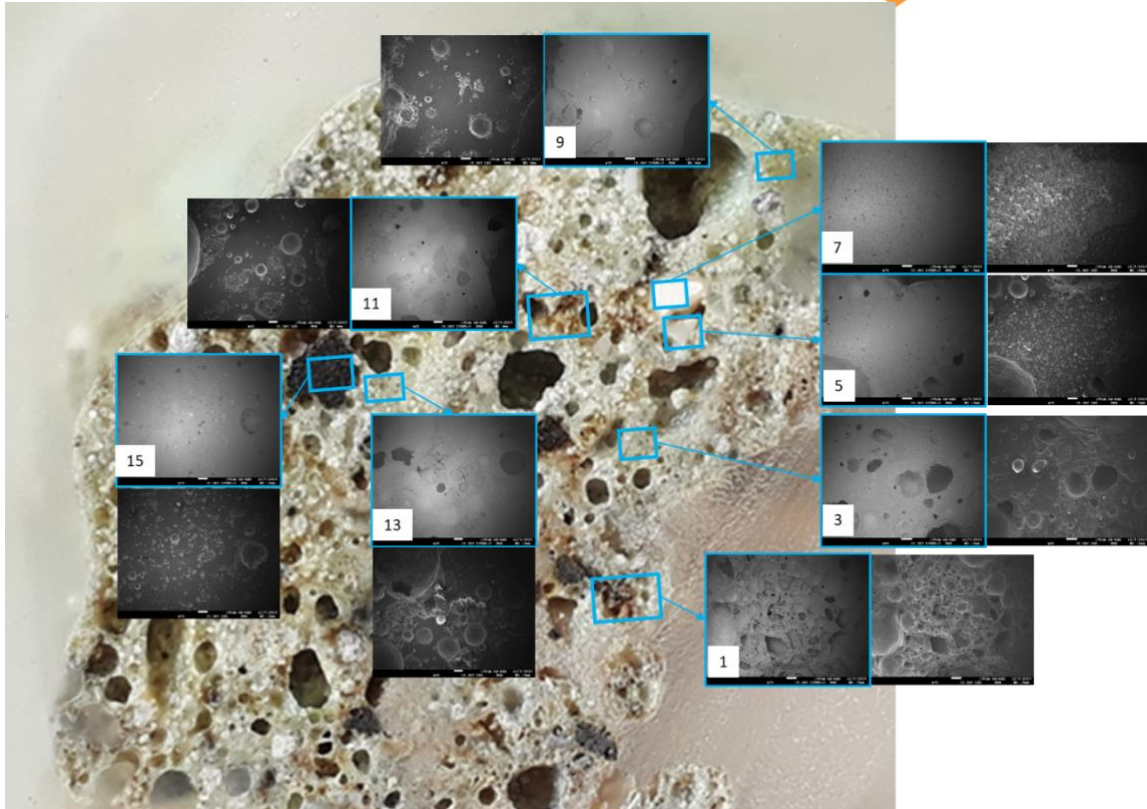


Figure 21. Cross section (and analyzed areas with BSE images) of the slag sample after the OXY28 combustion case

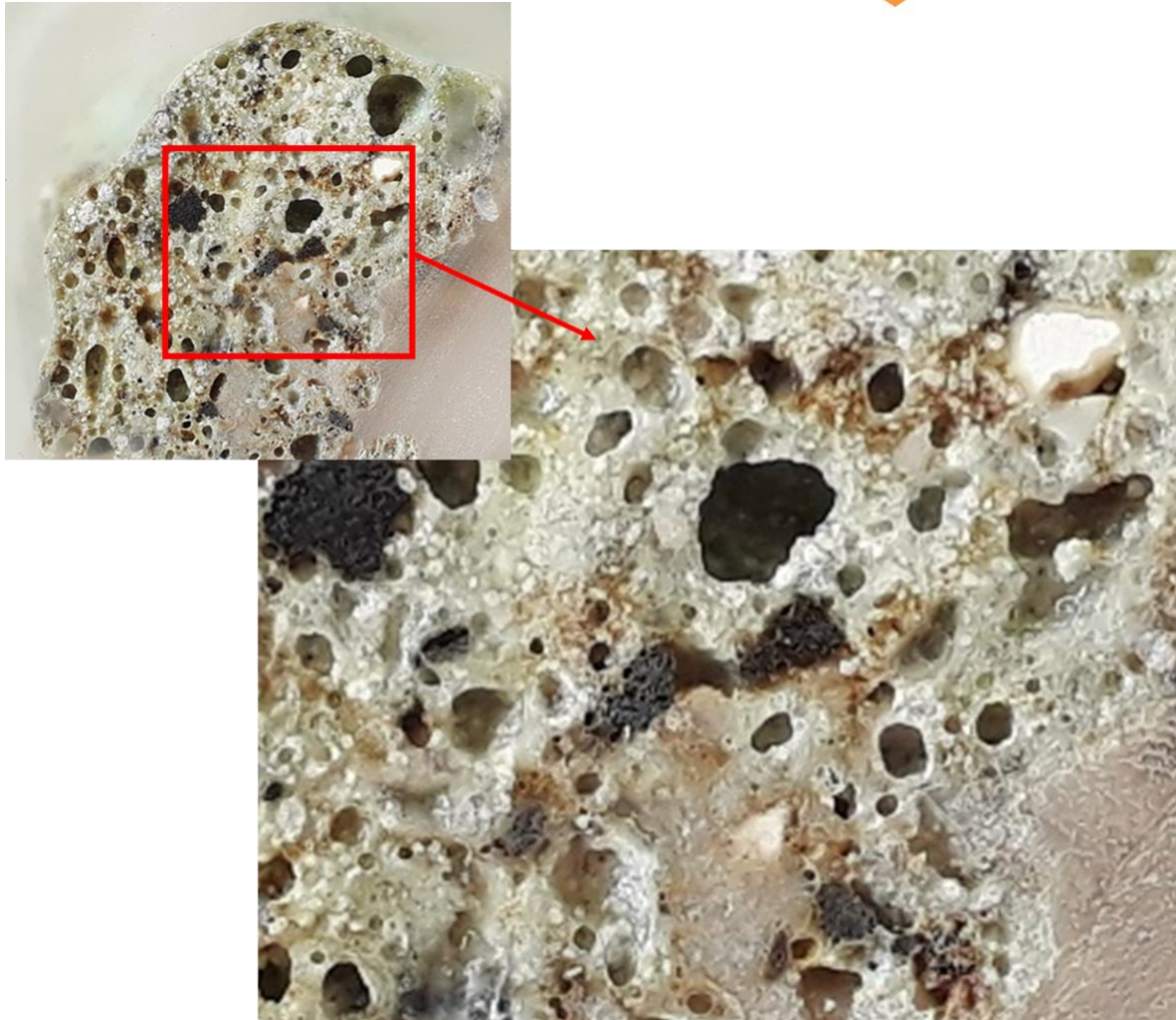
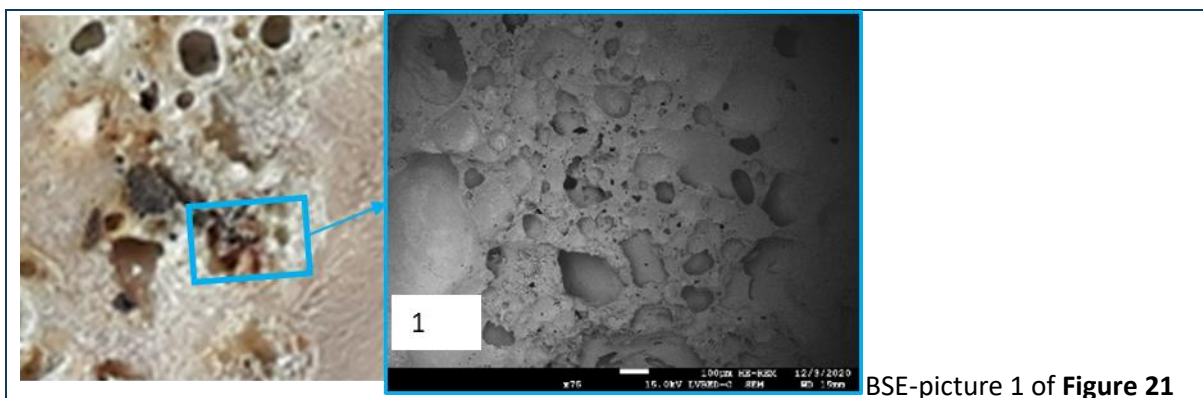


Figure 22. Detail image of the slag sample, optical structure

Figure 23 presents the results of a brownish area (number 1 in Figure 21) in the slag. This area is characterized by pores. The elements are homogeneously distributed. The two spectra show a high amount of Si and O, some Al, and a low amount of the alkalis Na, K, Ca, and also Mg. Spectrum 1 also shows a high proportion of Fe.



BSE-picture 1 of **Figure 21**

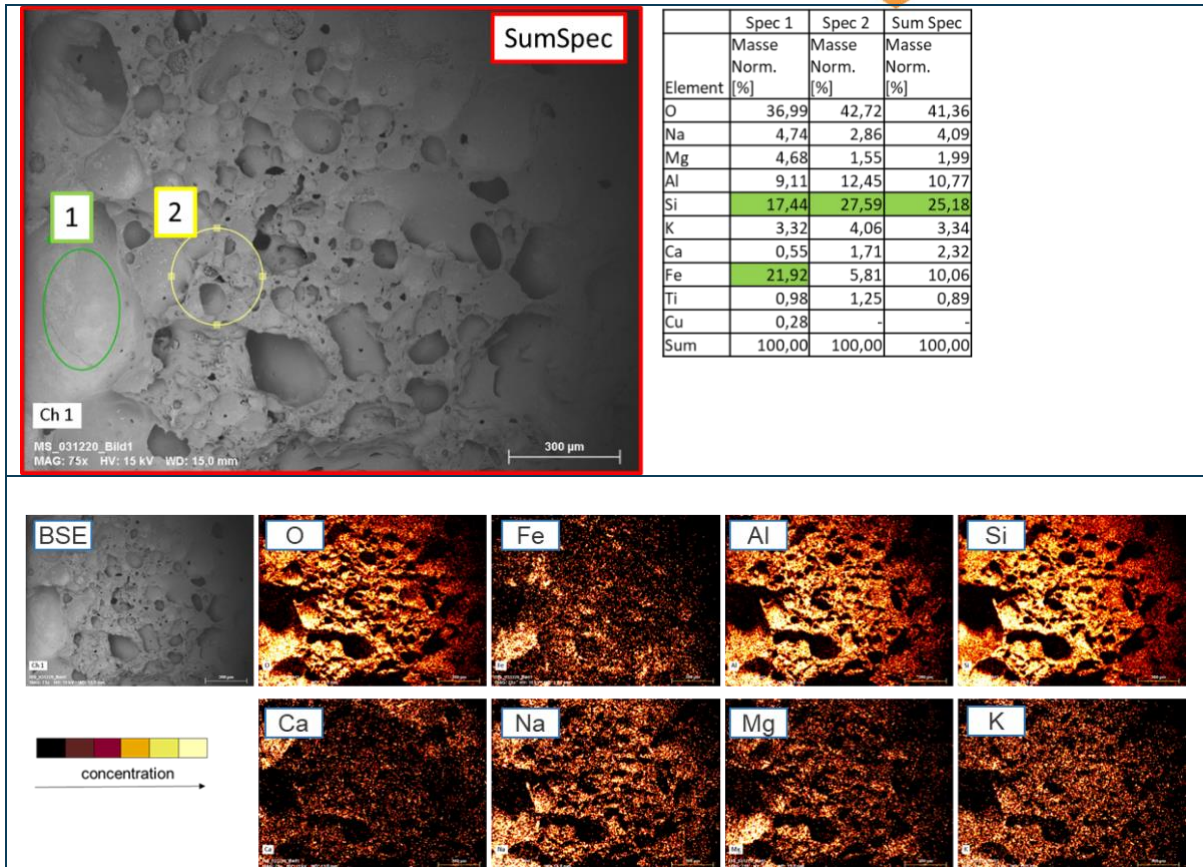
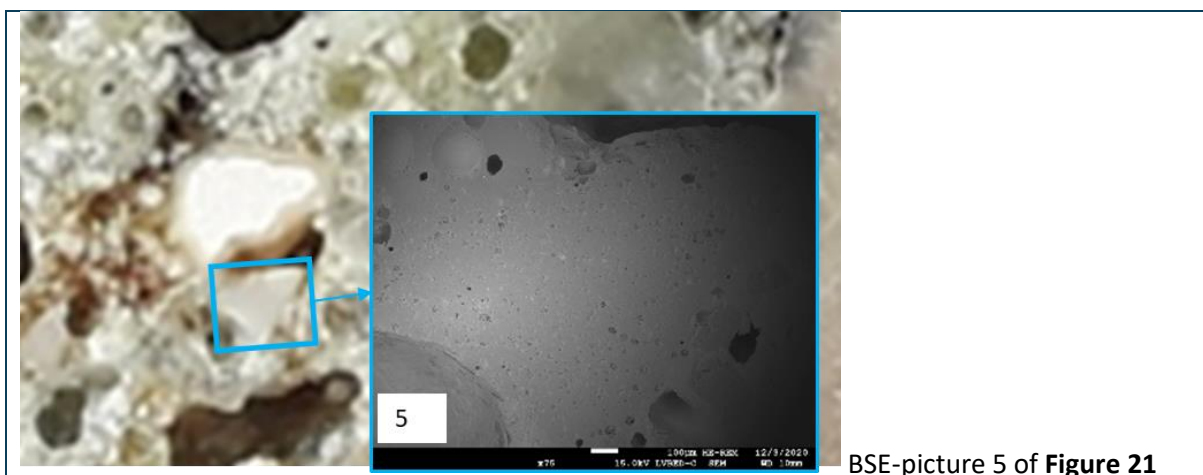


Figure 23. SEM/EDX results of the brownish area (number 1 in Figure 21) in the slag; above: BSE picture; middle: Spectra of two small areas (green 1 and yellow 2; semi-quantitative); below: element mappings

Figure 24 presents the results of area 5 in Figure 21 in the slag. This area shows a compact pore-free particle. The elements are homogeneously distributed (spectrum 1). To the side of the particle, a different composition (spectrum 2) can be seen. Spectrum 1 shows a high amount of Si and O, some Al, and a low amount of the alkalis Na, K, Ca, and also Mg. Spectrum 2 also shows a high amount of Ca, which indicates the presence of CaO.



BSE-picture 5 of Figure 21

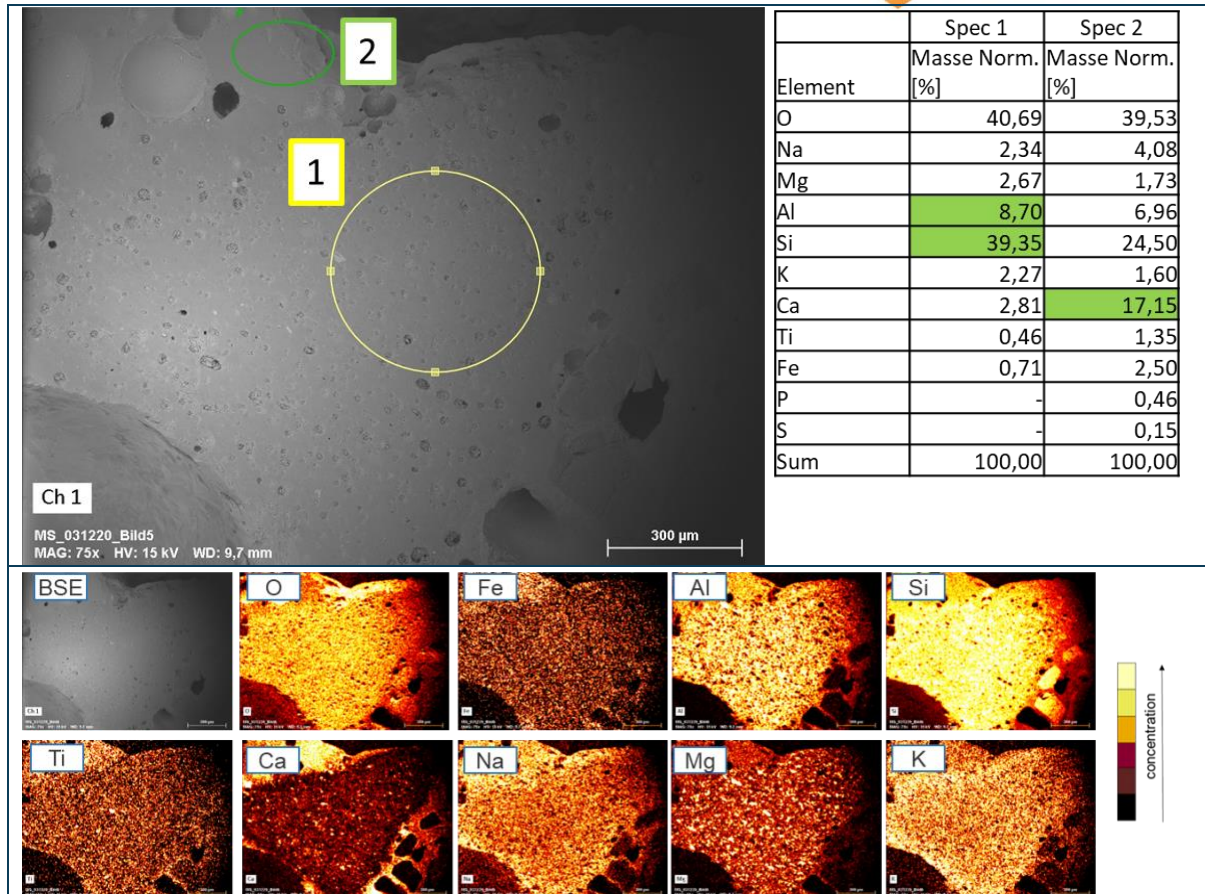
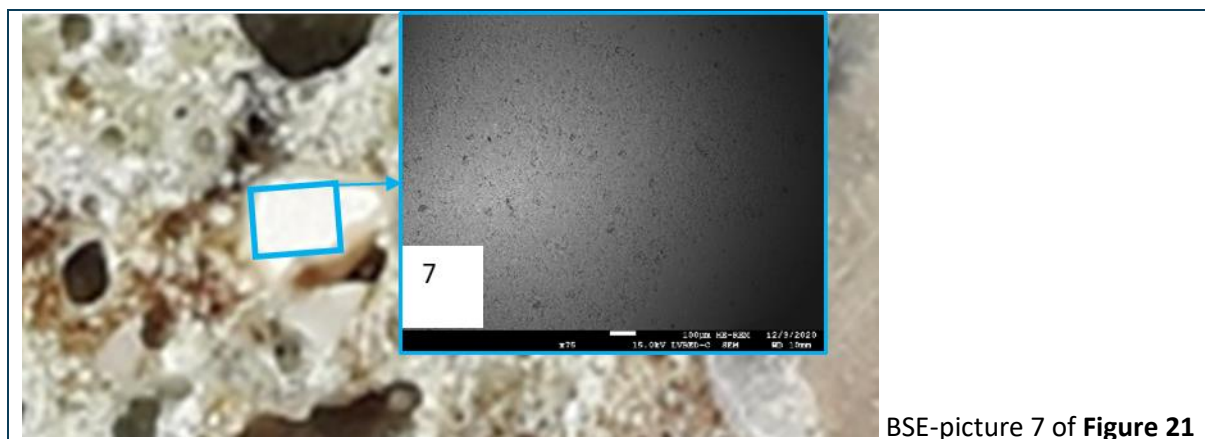


Figure 24. SEM/EDX results of area 5 in **Figure 21** in the slag; above: BSE picture; middle: Spectra of two small areas (green 2 and yellow 1; semi-quantitative); below: element mappings

Figure 25 presents the results of a white area (number 7 in **Figure 21**) in the slag. This area shows another compact pore-free particle. The elements are homogeneously distributed. Spectrum 1 shows again a high amount of Si, O, and Al and a low amount of the alkalis Na, K, and also Mg. Ca is present in a higher amount than the pore-free particle in **Figure 24** (Spec 1).



BSE-picture 7 of **Figure 21**

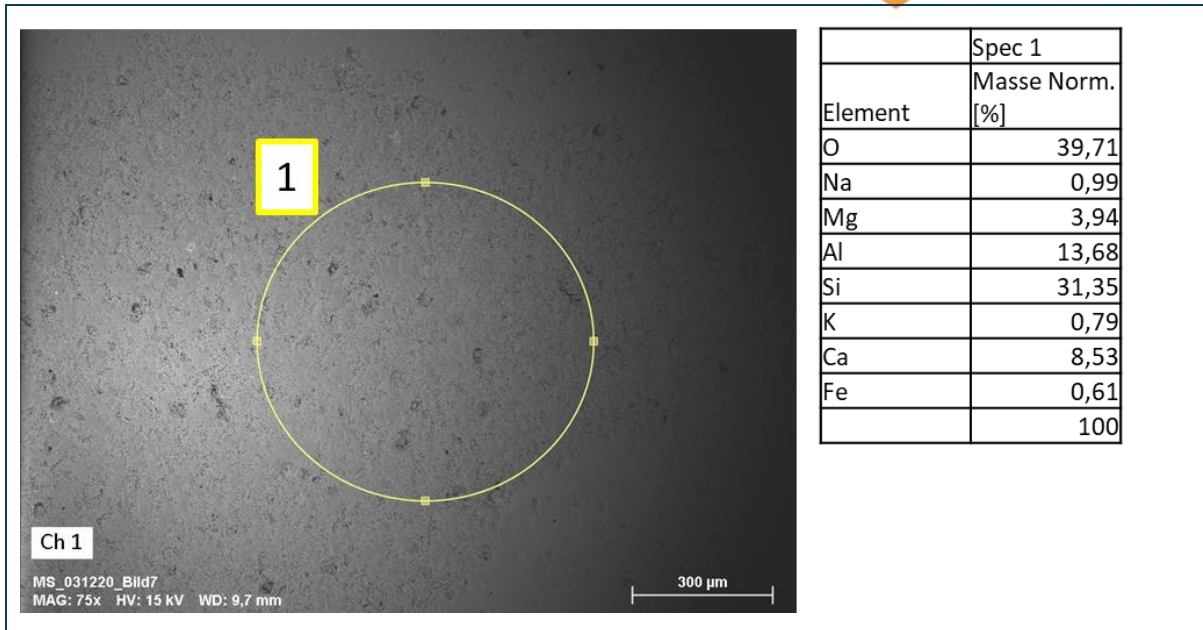


Figure 25. SEM/EDX results of a white area (number 7 in Figure 21) in the slag; above: BSE picture; below: Spectrum of one area (yellow 1; semi-quantitative)

Figure 26 presents the results of a black area (number 15 in Figure 21) in the slag. In this area, the elements are homogeneously distributed (O, Al, Si, Ca, Na). Some areas show a higher amount of Fe, Mg, and O.

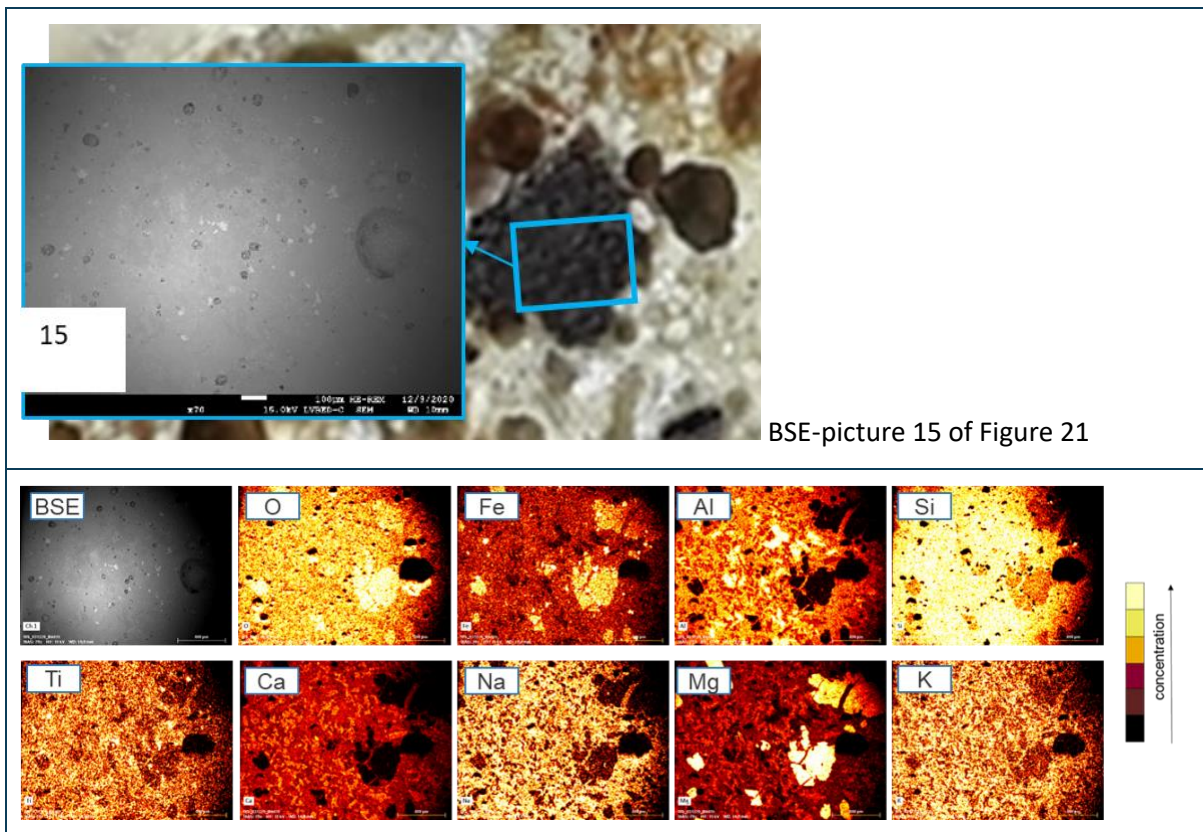


Figure 26. SEM/EDX results of a black area (number 15 Figure 21) in the slag; above: BSE picture; below: element mappings

Conclusions

The slag is mainly characterized by SiO as well as CaO contents. Alkalis are distributed in small proportions. There are inclusions of different compositions. The slag piece is formed by pores.

Analysis of solid samples during corrosion measurements

Air combustion

Sample ID	001	003	005	013	021	029	033	035	045	047	049
Time (HH:MM)	12:49	12:50	14:35	16:35	18:30	20:30	21:30	21:33	00:00	00:30	00:35

Proximate analysis	an	an	an	an	an	an	an	an	an	an	an
Moisture (wt%)	0,17	0,66	<0,1	<0,1	<0,1	<0,1	<0,1	0,65	0,10	0,49	0,13
Ash (wt%)	92,1	71,5	99,8	99,8	99,5	99,8	99,5	82,8	99,8	86,1	98,1

Carbon species	an	an	an	an	an	an	an	an	an	an	an
TOC (wt%)	<0,02	0,055	<0,02	<0,02	<0,02	<0,02	<0,02	<0,02	<0,02	0,030	<0,02
TIC (wt%)	1,89	6,03	0,044	0,045	0,041	0,086	0,037	3,68	0,018	3,31	0,529
CO ₂ (wt%)	6,94	22,1	0,161	0,167	0,152	0,315	0,135	13,5	0,065	12,1	1,94

Ultimate analysis	an	an	an	an	an	an	an	an	an	an	an
Cl (wt%)	1,81	2,76	0,011	0,010	0,011	0,013	0,013	11,0	0,014	13,0	0,869
H (wt%)	0,39	0,68	<0,1	<0,1	<0,1	<0,1	<0,1	0,50	<0,1	0,37	<0,1

Main elements	an	an	an	an	an	an	an	an	an	an	an
Al ₂ O ₃ (wt%)	10,7	2,31	2,69	2,58	2,88	2,90	2,77	3,22	2,52	4,02	8,13
BaO (wt%)	0,250	0,050	0,076	0,073	0,088	0,090	0,088	0,108	0,079	0,132	0,241
CaO (wt%)	31,6	53,9	5,15	6,05	5,85	6,48	6,29	39,8	6,10	33,6	18,2
Fe ₂ O ₃ (wt%)	2,43	0,693	0,562	0,661	0,799	0,821	0,763	1,23	0,720	1,34	2,07
K ₂ O (wt%)	3,07	3,60	1,35	1,25	1,29	1,23	1,21	6,34	1,12	7,96	1,88
MgO (wt%)	2,58	2,10	0,602	0,687	0,602	0,639	0,652	2,27	0,609	1,79	1,89
MnO ₂ (wt%)	0,169	0,098	0,030	0,029	0,034	0,035	0,036	0,110	0,033	0,102	0,097
Na ₂ O (wt%)	2,31	1,12	1,59	1,37	1,22	1,17	1,26	5,03	1,19	7,04	2,49
P ₂ O ₅ (wt%)	1,37	0,509	0,179	0,222	0,248	0,281	0,250	0,901	0,227	0,975	1,028
SO ₃ (wt%)	1,98	1,28	0,241	0,237	0,426	0,565	0,440	2,53	0,550	4,51	1,87
SiO ₂ (wt%)	34,4	5,86	86,7	86,6	87,1	85,6	85,4	8,06	85,4	9,72	57,3
SrO (wt%)	0,044	0,041	0,011	0,015	0,013	0,014	0,014	0,039	0,014	0,043	0,039
TiO ₂ (wt%)	1,98	0,344	0,346	0,327	0,450	0,508	0,484	1,46	0,439	1,64	1,56

Brief explanation:

- Loop seal samples: 005, 013, 021, 029, 033, 045
- Protective cyclone samples: 001, 049

- Bagfilter samples: 003, 035, 047

OXY28 (Oxy-fuel combustion with 28 vol% inlet O₂)

Sample ID	145	147
Time (HH:MM)	01:00	01:30

Proximate analysis	an	an
Moisture (wt%)	<0,1	<0,1
Ash (wt%)	99,8	99,8

Carbon species	an	an
TOC (wt%)	<0,02	<0,02
TIC (wt%)	0,056	0,075
CO ₂ (wt%)	0,204	0,276

Ultimate analysis	an	an
Cl (wt%)	0,022	0,024
H (wt%)	<0,1	<0,1

Main elements	an	an
Al ₂ O ₃ (wt%)	4,35	4,44
BaO (wt%)	0,142	0,142
CaO (wt%)	11,4	11,5
Fe ₂ O ₃ (wt%)	1,74	1,69
K ₂ O (wt%)	1,24	1,30
MgO (wt%)	1,26	1,28
MnO ₂ (wt%)	0,060	0,062
Na ₂ O (wt%)	2,45	2,51
P ₂ O ₅ (wt%)	0,548	0,563
SO ₃ (wt%)	0,385	0,376
SiO ₂ (wt%)	75,2	74,3
SrO (wt%)	0,026	0,026
TiO ₂ (wt%)	0,879	0,868

Brief explanation:

- Loop seal samples: 145, 147